SCIEPublish

Article

Thermogravimetric Study of the Oxidation Behavior of the Cantor's Alloy at 1000 °C and Beyond

Patrice Berthod [1,2,*], Lionel Aranda [2]

[1] Faculty of Sciences and Technologies, Victor Grignard Campus, 54239 Vandoeuvre-lès-Nancy, France
[2] Jean Lamour Institut, 2 allée André Guinier, Artem Campus, 54011 Nancy, France; lionel.aranda@univ-lorraine.fr (L.A.)

* Corresponding author. E-mail: patrice.berthod@univ-lorraine.fr (P.B.)

Received: 30 December 2023; Accepted: 18 March 2024; Available online: 17 April 2024

ABSTRACT: A polycrystalline Cantor alloy, equimolar in Co, Cr, Fe, Mn and Ni, was cast. It was subjected to oxidation in a thermo-balance in a flow of synthetic dry air, at 1000, 1050, 1100 and 1150 °C. The mass gain was globally parabolic but rather irregular. The parabolic constants, ranging from 55 to 700 × 10^{-12}·g^2·cm^{-4}·s^{-1}, are much higher than for a chromia-forming alloy. They obey an Arrhenius law with an activation energy equal to 270 kJ/mol. The external oxide scales formed are composed of an outer part made of manganese oxide and an inner part made of (Cr,Mn) oxide containing a thin internal layer of chromia. The Mn and Cr-depleted depths and the Mn and Cr masses lost by the alloy increase with the oxidation temperature. Cr-rich acicular particles precipitated in subsurface at 1100 °C and internal oxidation along the grain boundaries are present in the whole thickness of the sample oxidized at 1150 °C. Oxide spallation occurred during the cooling, at temperatures in the 200–350 °C range, only for the alloys oxidized at 1050 and 1100 °C. Not too thick scale (1000 °C) or deep internal oxidation (1150 °C) may be favorable for scale adherence.

Keywords: Cantor alloy, Equiatomic CoCrFeMnNi composition, Elevated temperatures, Thermogravimetry follow-up, Kinetic analysis, Metallographic characterization

1. Introduction

The acceleration of the development of High Entropy Alloys (HEAs) and of the associated multicomponent alloys took place in 2004 with the investigations of Cantor et al. [1,2] and of Yeh et al. [3–6]. The equiatomic CoCrFeMnNi composition attracted particular attention. Such alloys were envisaged for many types of applications, including for metallic components working at high temperatures. At temperatures higher than 500 °C, such alloys may encounter rather fast dry oxidation if they are exposed to air or other oxygen-containing gases [7,8]. Due to the high melting points of the elements of their composition (for all, T_m > 1455 °C, except Mn: 1246 °C), the equimolar CoCrFeMnNi alloys may be considered for constituting the base of new high temperature alloys able to replace some superalloys [9,10]. Such alloy composition limits the dependence on expensive and critical elements (Co, Ni) thanks to their partial substitution by much common metals (Fe, Mn). Alloys with such equimolar base, and efficiently strengthened by MC carbides, were recently investigated [11–13]. Prior to mechanical characterization at elevated temperature, it is important to explore the oxidation behavior of equimolar CoCrFeMnNi alloys at the elevated temperatures which are typical of the thermal conditions that superalloys encounter in service.

The oxidation behavior of equimolar CoCrFeMnNi alloys was earlier explored at temperature ranging from 500 to 800 °C, for example by Laplanche et al. [14], Stephan-Scherb et al. [15] or Bürckner et al. [16]. In contrast, there are seemingly very few oxidation studies which were carried out at temperatures beyond 1000 °C. One can only cite the recent work of Jiang et al. [17] who tested such alloys at temperatures up to 1150 °C. They performed only exposures to air in a furnace with interruptions at different times for weighing the specimen mass after each duration. The present work was carried out for better specifying the oxidation kinetic of a cast equimolar CoCrFeMnNi alloy. A recording of the mass variation during oxidation (use of a thermo-balance), followed by the analysis of the oxide scale spallation

https://doi.org/10.35534/htm.2024.10002

during the cooling, aims to complete this interesting former recent investigation with more accurate quantitative data. The investigation was extended to the analysis of the corrosion products formed and of the characterization subsurface degradation induced by oxidation. These observations were compared to previous studies.

2. Materials and Methods

An alloy with equal atomic contents in Co, Cr, Fe, Mn and Ni was elaborated by induction melting (CELES furnace (Lautenbach, France), 100 kHz, 5 kV). A mixture of pure elements (Alfa Aesar (Haverhill, USA); purity > 99.9% for each of them) was prepared and cast in an inert atmosphere made of 300 millibars of pure Argon. The weight of the obtained ingot was 40 grams approximately. It was cut in several parts using a metallographic saw. One part was prepared to serve as a metallographic sample (mounted, ground and polished), for the control of the chemical composition and of the single-phased microstructure: the first one well corresponds to the targeted composition (better than ± 1 at.% for all elements), and the second one is really constituted of a single FCC solid solution. Four other parts were prepared to obtain (10 mm × 10 mm × 3 mm) parallelepipeds which were ground with SiC papers up to the #1200 grade.

The four parallelepipeds were tested in isothermal oxidation, using a TGA92 thermo-balance from SETARAM (Caluire-et-Cuire, France), during 50 h, in a 1.5 L/h flow of synthetic dry air (80%N_2–20%O_2), at 1000, 1050, 1100 or 1150 °C. The heating rate to reach these temperatures of isothermal stage of oxidation was + 20 °C per minute. The cooling rate from the isothermal stage down to room temperature was −5 °C per minute. The mass gain values were exploited to plot two types of curves: either the mass gain versus time (constant temperature) for the isothermal oxidation part, or the mass variation versus temperature during the cooling starting at the end of the post isothermal stage.

After the tests, the oxidized specimens were carefully taken out of the alumina-covered platinum support. They were first subjected to X-ray diffraction (XRD), using a D8 Advance diffractometer from BRUKER (Billerica, USA) (Cu K_α, λ = 15.406 nm) to get first data about the nature of the oxidation products formed. After that, they were prepared for metallography. They were embedded in cold resin system. The obtained mounted samples were thereafter cut in two halves and ground up to 1200-grit SiC paper. After ultrasonic cleaning, they were polished with 1-µm hard particles added to a rotating textile disk. The obtained mirror-like cross-sectional samples were then characterized by electron microscopy. Imaging with the JSM-6010LA scanning electron microscope (SEM) from JEOL (Tokyo, Japan) was done using the back scattered electrons mode (BSE), and the chemical analysis (full frame, spot, concentration profiles, elemental mapping) was carried out using the energy dispersive spectrometer (EDS) attached to the SEM.

3. Theory/Calculation

The isothermal mass gain values may lead to various curve shapes: mainly linear (no alloy protection against oxidation by the formed external oxides, thus fast oxidation) or parabolic (more or less efficient protection of the alloy by a continuous external oxide scale, thus oxide growth obeying the Wagner's law).

In the first case, the value of the kinetic linear constant K_L involved in the (E1) equation will be specified, as the slope of the mass gain curve plotted versus time. In the second case, this is the kinetic parabolic constant K_P, which features in the (E2) equation, which will be deduced. This was done by plotting the mass gain versus the square root of time and by determining the slope of the straight line representing mass gain in this other representation mode.

Finally, since different values of the K_L and/or K_P constants are expected to be obtained, it will be verified if these constants obey or not an Arrhenius law (E3). In such case, the slope of the straight line resulting of the plot, versus the reciprocal temperature 1/T (K^{-1}), of ln(K_L/g cm^{-2}·s^{-1}) or ln(K_P/g^2·cm^{-4}·s^{-1}), leads to the value of the activation energy Q.

$$\frac{d(\frac{\Delta m}{S})}{dt} = K_L \quad \text{(E1)} \qquad \frac{d(\frac{\Delta m}{S})}{dt} = \frac{K_P}{\frac{\Delta m}{S}} \quad \text{(E2)} \qquad K_L \text{ or } K_P = Constant \times e^{\frac{-Q}{R \times T}} \quad \text{(E3)}$$

In these formulas $\frac{\Delta m}{S}$ is the mass gain by surface unit area (unit: g·cm^{-2}) due to oxidation, t is time counted from the beginning of the isothermal stage (unit: s), K_L is the linear constant which characterizes the kinetic transient mass gain rate (unit: g·cm^{-2}·s^{-1}), K_P is the parabolic constant (unit: g^2·cm^{-4}·s^{-1}) which characterizes the mass gain rate when its kinetic obeys the Wagner's law, Q is the activation energy (unit: J·mol^{-1}) featuring in the Arrhenius law (two Q values, one for K_P and one for K_L), R is the constant of the state law of perfect gases (value: 8.314 J·mol^{-1}·K^{-1}), and T is the absolute temperature of oxidation (unit: K).

4. Results

4.1. Thermogravimetry

4.1.1. Isothermal Oxidation

The obtained mass gain curves are plotted together in a single graph in Figure 1, either versus time (left) or versus the square root of time (right). Some of the mass gain curves plotted versus time are a little irregular (1050, 1100 and 1150 °C). Each of them includes a jump (or several jumps) of mass gain. It results from a temporary fast local oxidation of a part of surface which is denuded because a local scale unsticking due to oxide growth stresses. Nevertheless, one can consider that all curves are globally parabolic, at least by parts. One can see that the higher the test temperature the faster the global kinetic, as illustrated by the values of mass gain after the 50 h of isothermal oxidation presented in Table 1 (first column of results). The mass gain was also plotted versus the square root of time, but only on the curve part before the first jump. Indeed, after local re-oxidation, the scale growth cannot be longer homogeneous. Only the mass gains recorded during the first 20 h of isothermal oxidation are taken into account. Despite that no jump in mass gain was observed during oxidation at 1000 °C, the corresponding curve was also shortened to keep only the first 20 h, for treatment homogeneity. The obtained ($m = f(t^{1/2})$) curves—presented in Figure 1 (right)—are rather straight but one can observe a slight curvature oriented upwards, suggesting that a small contribution of linear oxidation may also exist. The average slopes of these ($m = f(t^{1/2})$) curves were exploited to estimate the values of the parabolic constant. These values are given in Table 1 (second column of results). The plot of the K_P values according to the Arrhenius scheme (Figure 2) gives a rather good point alignement of the points corresponding to the four temperatures. The slope of the obtained straight line, multiplied by $-8.314\ J{\cdot}mol^{-1}{\cdot}K^{-1}$, leads to the following value of activation energy: $270\ kJ{\cdot}mol^{-1}$.

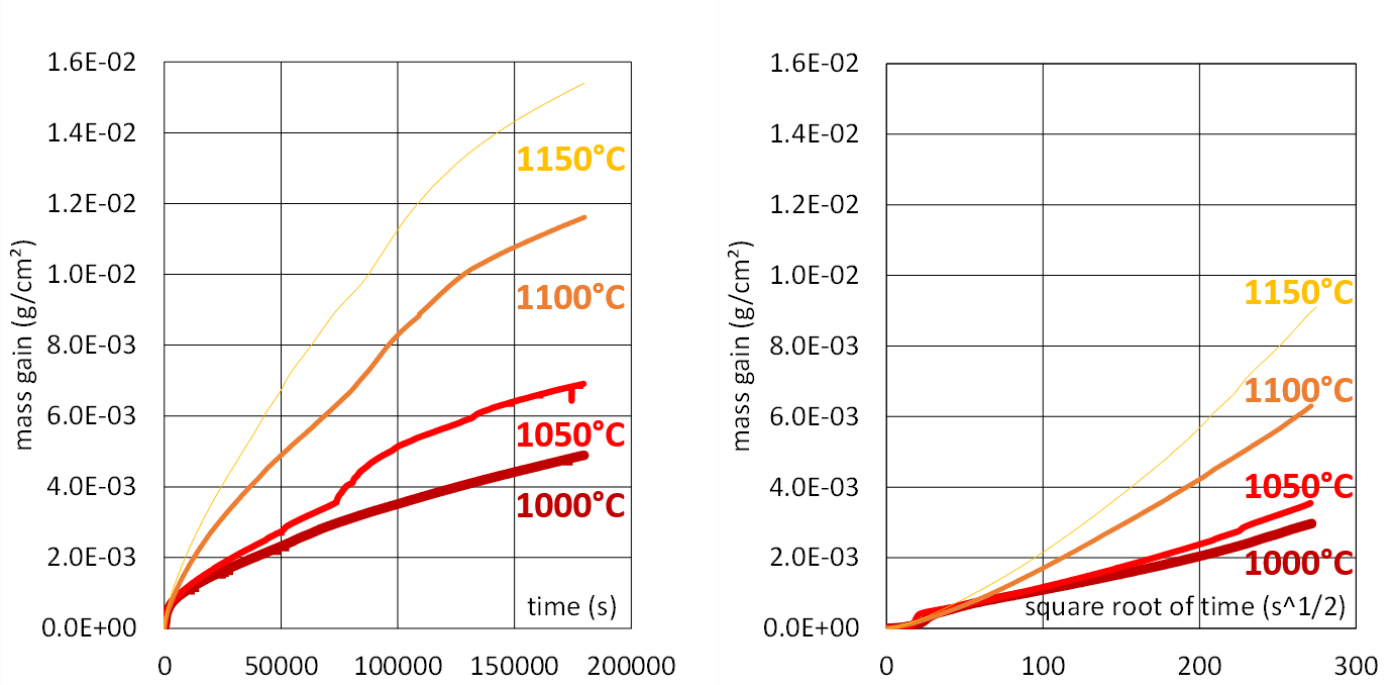

Figure 1. The four obtained mass gain curves (left: plotted versus time, right: plotted versus the square root of time).

Table 1. Values of the final isothermal mass gains and of the parabolic constants.

Temperature (°C)	Isothermal Mass Gain (mg/cm²)	*Kp* Value ($\times 10^{-12}$ g²·cm⁻⁴·s⁻¹)
1150	15.4	700
1100	11.6	325
1050	6.9	85
1000	4.9	55

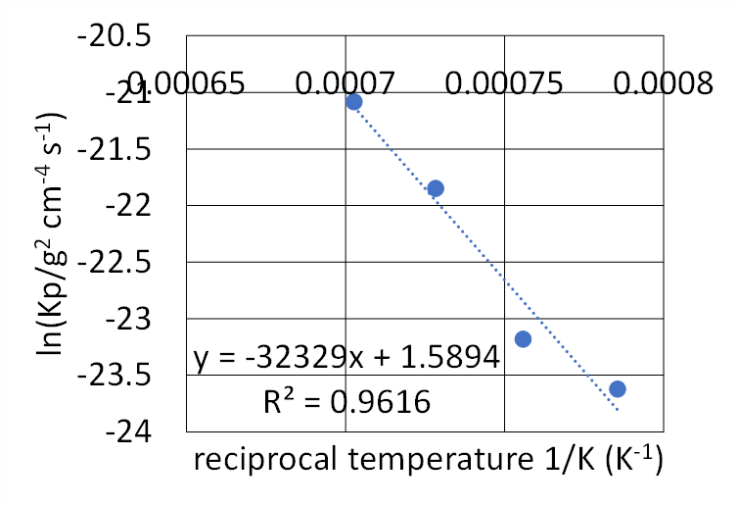

Figure 2. Arrhenius plot of the K_P values.

4.1.2. Oxide Scale Spallation during Cooling

The thermogravimetry results obtained for the four tests were also exploited, to observe the oxide scale spallation phenomena during the cooling. This was done by plotting, versus temperature, the mass variations during the cooling parts of the curves (Figure 3). Obviously, no particular behavior of the mass gain is observed during the cooling of the specimens oxidized at 1000 °C or at 1150 °C. The continuous small decrease in mass near the end of cooling is due to the increase in air density which induces an apparent mass diminution. In contrast, the irregular decrease in mass observed for the alloy oxidized at 1050 and at 1100 °C (Figure 3) when temperature decreases below 337 and 200 °C respectively (Table 2, first column of results), reveals repeated losses of oxide scale. In these cases significant oxide mass losses are noticed (Table 2, second column of results).

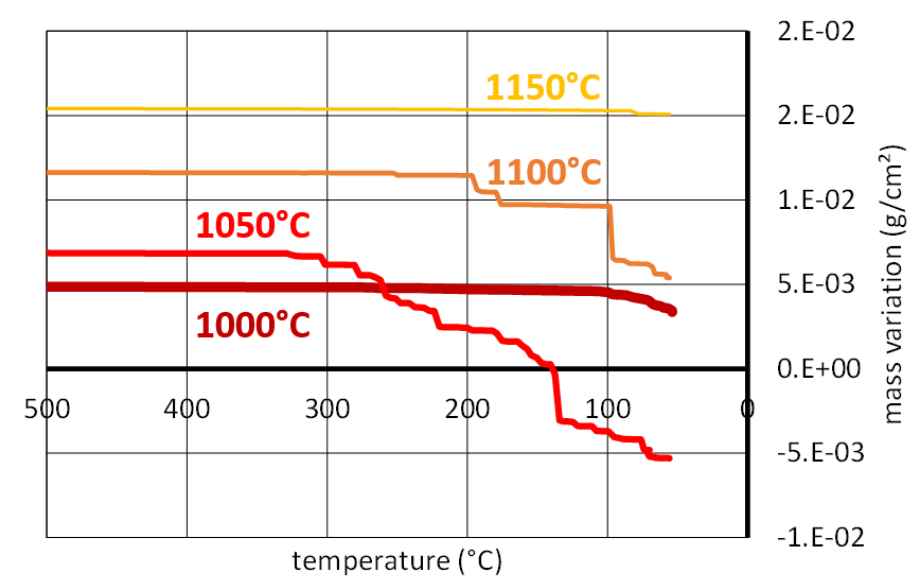

Figure 3. The four mass variation curves plotted versus temperature for the cooling part.

Table 2. Values of two parameters describing the spallation phenomenon and its severity.

Temperature of Isothermal Oxidation (°C)	Start Temperature of Oxide Scale Spallation (°C)	Mass Loss Due to Oxide Scale Spallation (mg/cm²)
1150	No spallation evidenced	
1100	200	6.1
1050	337	12.1
1000	No spallation evidenced	

4.2. Post-mortem Metallographic Characterization after Oxidation at 1000, 1050 and 1100°C

The obtained XRD diffractograms (two of them presented in Figure 4 as examples) revealed that the oxide scales were rather complex, with the presence of several types of oxides. Many of them involve manganese (MnO_2, Mn_3O_4). Chromium took part to oxidation too, with the formation of chromia (Cr_2O_3) and of a spinel oxide of Mn and Cr: $MnCr_2O_4$).

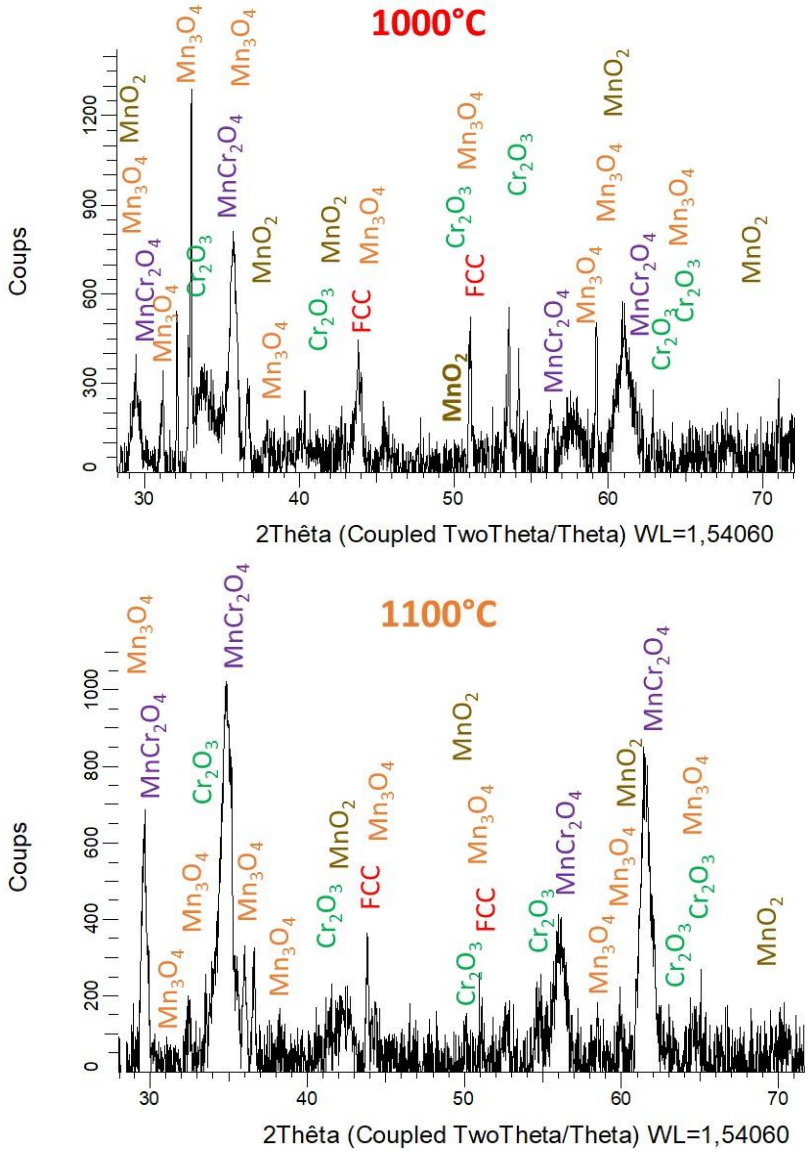

Figure 4. Examples of diffractograms acquired by XRD on the oxidized surfaces (top: specimen oxidized at 1000 °C, bottom: 1100 °C).

After cross-sectional preparation, the obtained metallographic samples were examined using electron microscopy. The oxidized states of the alloys exposed to 1000, 1050 and 1100 °C are illustrated in Figure 5. For the three samples a continuous oxide scale developed all around the alloy. As the kinetic of mass gain increased with temperature, the average thickness of oxide scale should be greater for a greater temperature. Unfortunately such oxide thickness comparison between the three alloys cannot be done since scale spallation occurred for the alloys oxidized at 1050 and 1100 °C. Other comparisons can be done, between the degradation states in subsurface. The specimens oxidized at 1050 and 1100 °C present porosities (shown by arrows and the **o** symbol) over a depth of 50–100 µm from the interface with the oxide scale, in contrast with the specimen oxidized at 1000 °C for which no such subsurfacic porosities can be evidenced. Specifically for the specimen oxidized at 1100 °C, below the part affected by porosities one can see an inner alloy part which is affected by the presence of acicular dark precipitates (shown by arrows and the ◊ symbol). Spot analyses revealed, in these particles, high concentrations in chromium, nitrogen and maybe oxygen.

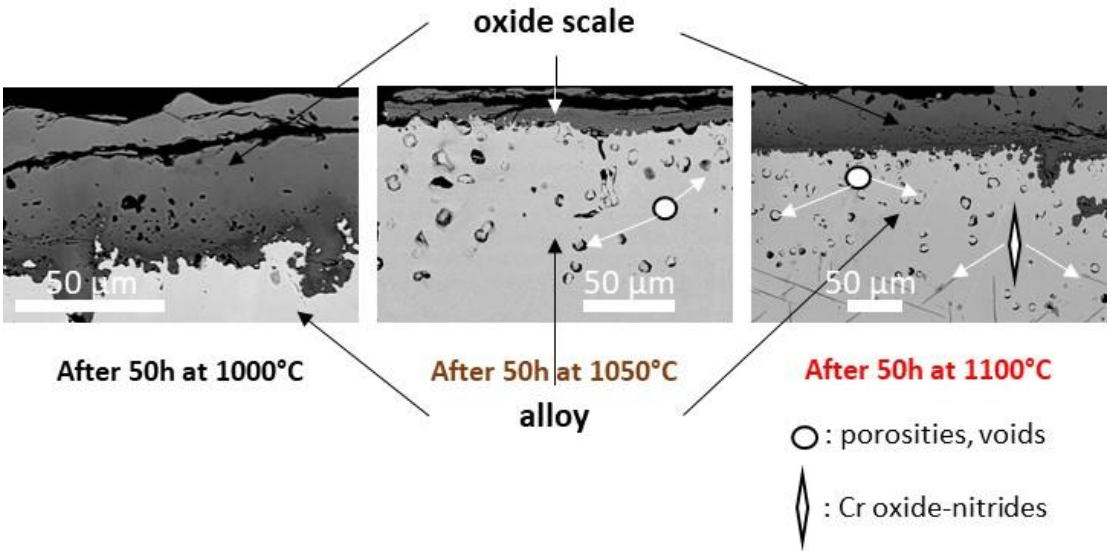

Figure 5. Micrographs of the surface states and of the subsurface degradated state of the alloys oxidized in air at 1000, 1050 and 1100 °C.

Elemental mapping was run on areas covering the oxide scales and the subsurfaces affected by oxidation. Two examples are given in Figures 6 and 7, in the case of the specimen oxidized at 1000 °C and for the one oxidized at 1100 °C, respectively. Concerning the specimen oxidized at 1000 °C (Figure 6) one can see that the composition of the oxide scale is not homogeneous. The scale part close to the interface with the alloy is rich in Cr while the main part of the scale is much richer in Mn than in Cr. One can also see that the outermost part of the subsurface is impoverished in Cr and in Mn. The Mn-depleted zone is more visible than the Cr-depleted one.

Analogous qualitative comments are applicable for the specimen oxidized at 1100 °C (Figure 7): one observes the repartition of Cr and Mn through the oxide scale, and the Cr-depleted and Mn-depleted zones in the subsurface are better evidenced. This allows seeing that the depletion in Mn is significantly deeper than the depletion in Cr. In addition, one can observe the high Cr concentration in the acicular particles precipitated deeper.

To get more quantitative data about the element distribution across the oxide scales and in the subsurface, EDS profiles were acquired perpendicularly to the external face (Figure 8). These profiles confirm the observations made above with the X-maps: a significant outermost part of the scale is constituted of an oxide of manganese (possibly MnO_2) while the inner part is an oxide in which Cr and Mn co-exist. In the innermost part of this inner part chromium predominates.

EDS profiles were acquired from the oxide scale/alloy interface toward the bulk to quantitatively specify the elemental distribution in the subsurface (Figure 9). Severe impoverishment in Mn and Cr can be noticed, more for Mn than for Cr. The contents in these elements in the alloy close to the interface with the scale are significantly lower for Mn than for Cr, and the depleted zones are also deeper for Mn than for Cr.

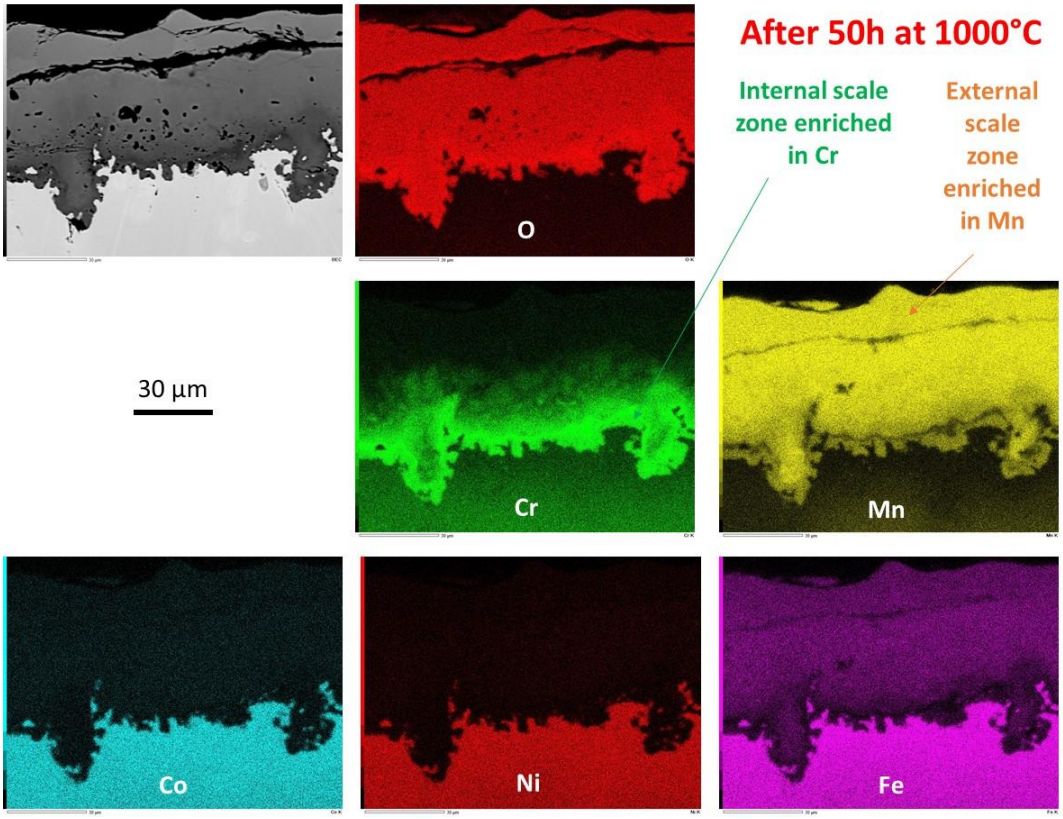

Figure 6. EDS X-map revealing the elemental distribution in the oxide scale and in the subsurface affected by oxidation for the specimen oxidized at 1000 °C.

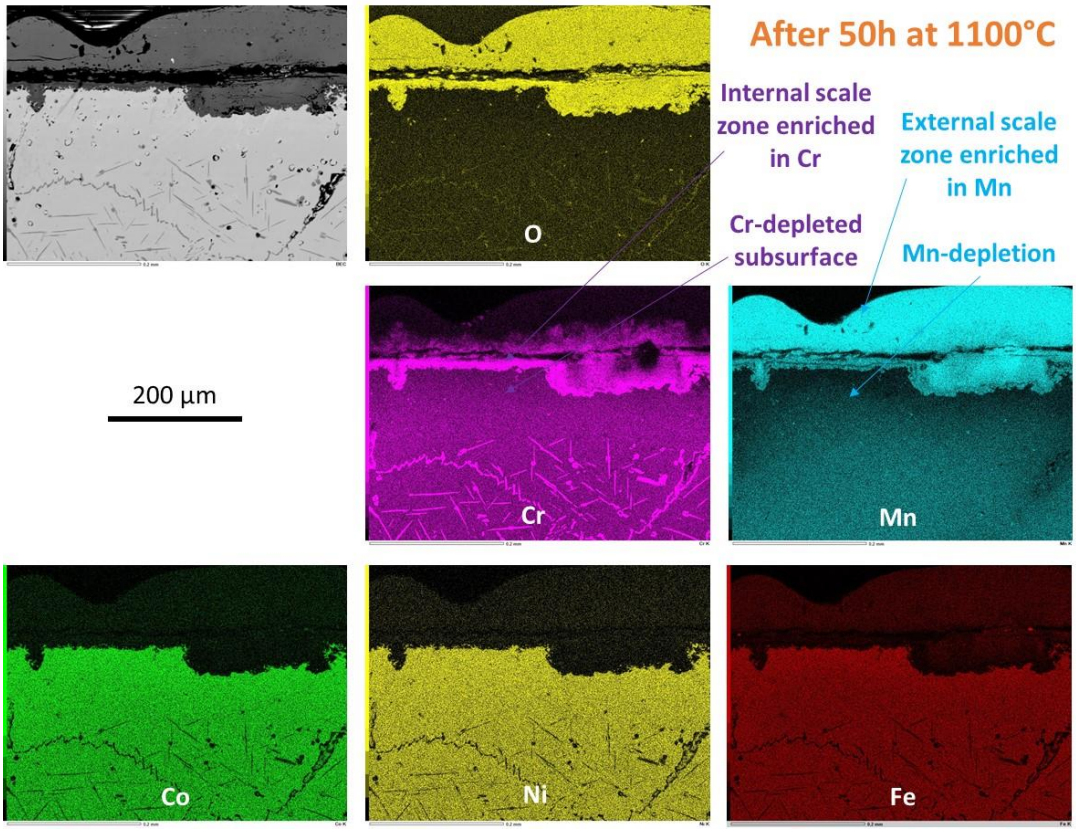

Figure 7. EDS X-map revealing the elemental distribution in the oxide scale and in the subsurface affected by oxidation for the specimen oxidized at 1100 °C.

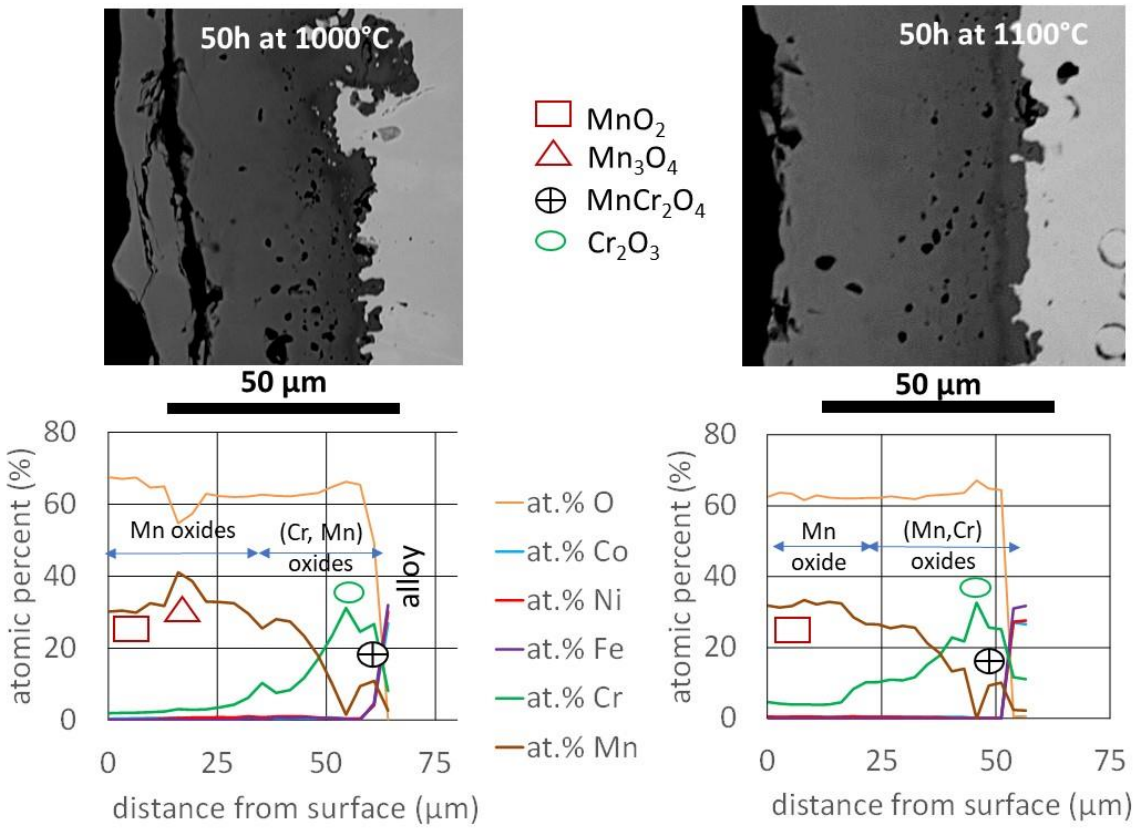

Figure 8. Concentrations profiles acquired through the external oxide scale covering two of the oxidized specimens.

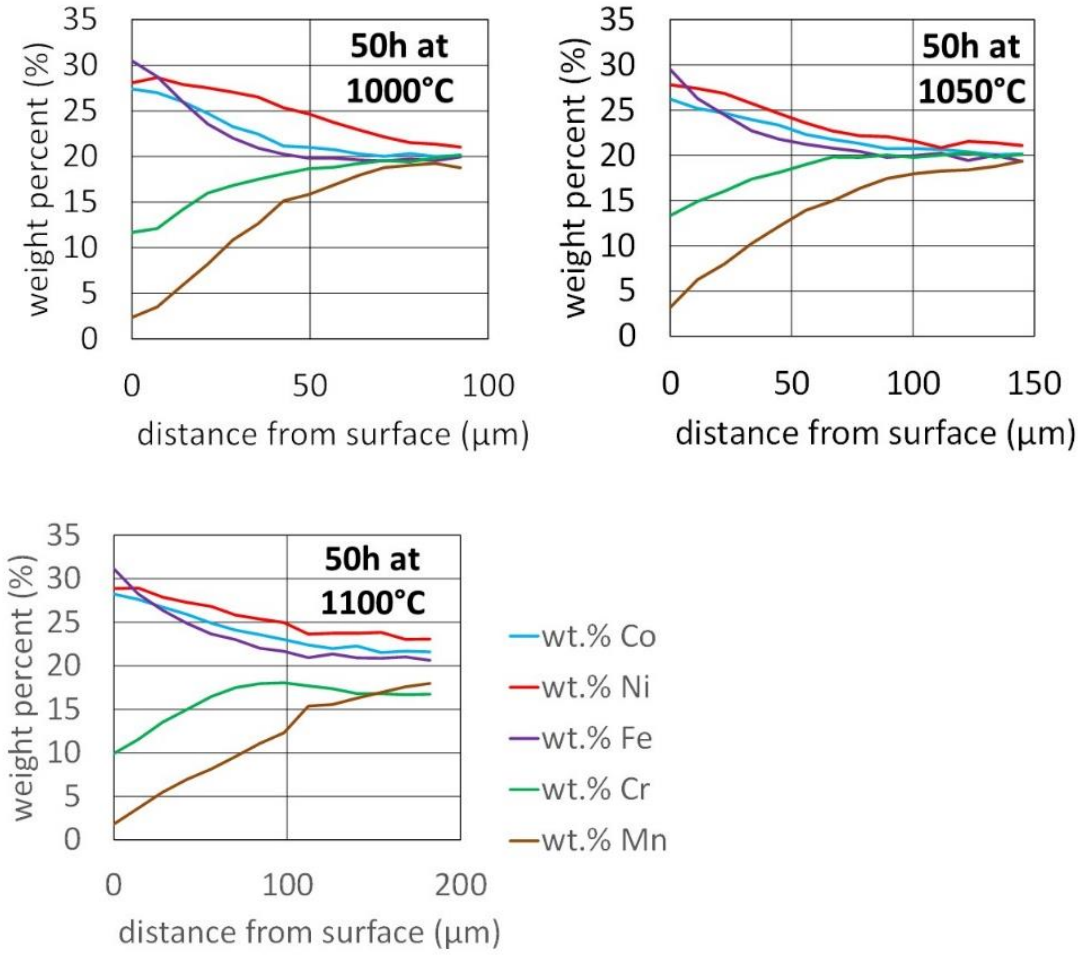

Figure 9. Concentration profiles acquired in the subsurface, revealing the impoverishment in Mn and Cr.

4.3. Post-mortem Metallographic Characterization after Oxidation at 1150 °C

The specimen exposed to 1150 °C was severely affected. Thick oxide scales formed on surface and oxidation took place also through the specimen. The external and internal states are illustrated in Figure 10 (SEM/BSE image) and in Figure 11 (EDS X-maps). One can observe the same Cr-rich and Mn-rich zones in the oxide scales formed at 1000, 1050 and 1100 °C, as well as in the internal oxidized zones. One can also see the extensions of the Cr-depleted and Mn-depleted zones in alloy from the external faces along the oxidation penetration through the specimen.

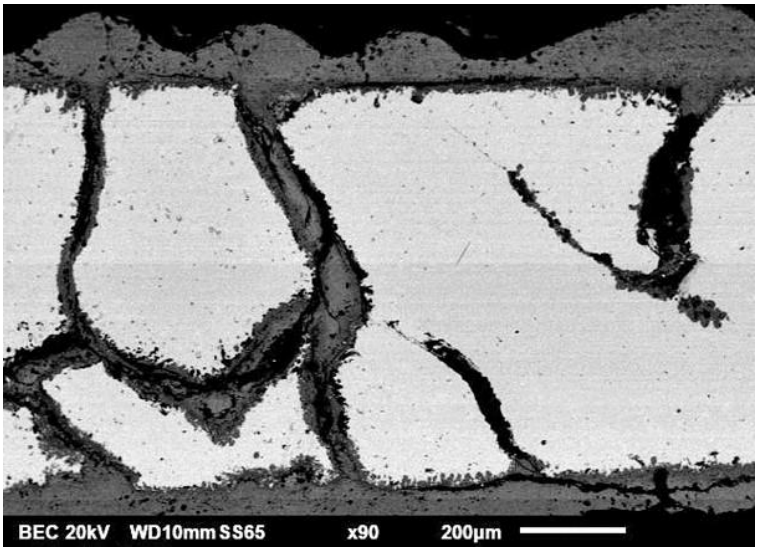

Figure 10. External and internal states of the alloy oxidized at 1150 °C.

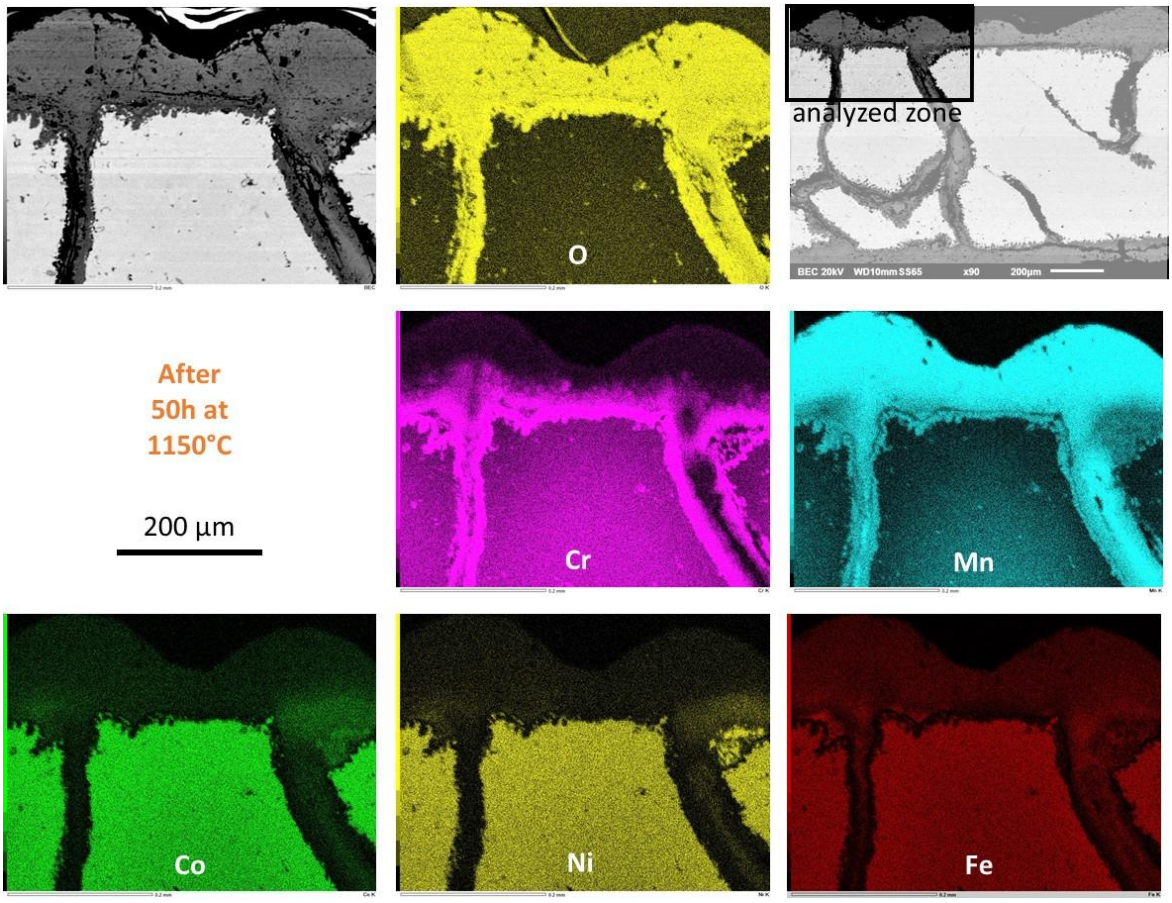

Figure 11. Elemental distribution on an area covering the oxide scale and the subsurface of the alloy oxidized at 1150 °C.

The chemical compositions close to the interface with the oxide scales were also measured for the specimen oxidized at 1150 °C. The results are added, in Table 3, to the ones measured for the specimens oxidized at 1000, 1050 and 1100 °C. There is no systematic trend versus temperature. All the measured Cr-depleted and Mn-depleted depths

are gathered in Table 4: the depleted depths increase with temperature and, for a given temperature, the Mn-depleted zones are more extended than the Cr-depleted ones. Full frame EDS analysis on subsurface areas covering the depleted zones allowed specifying the Mn and Cr quantities lost by the specimens, by comparison with the initial compositions. The results are presented in Table 5. Unsurprisingly the loss per surface unit area is higher for Mn than for Cr, and these losses increase with temperature.

Table 3. Chemical compositions in alloy close to the interface with the oxide scale.

Weight Contents in Alloy Close to the Oxide Scale	(wt.%)	Cr	Mn	Fe	Co	Ni
1150 °C	Average	10.43	1.99	30.43	27.86	29.28
	Std dev.	2.77	0.56	0.95	1.07	1.35
1100 °C	Average	11.09	2.26	30.47	27.38	28.79
	Std dev.	0.89	0.35	0.56	0.52	0.59
1050 °C	Average	14.29	3.84	26.03	25.99	29.89
	Std dev.	3.02	1.50	3.89	1.00	3.46
1000 °C	Average	10.80	2.07	31.04	27.58	28.52
	Std dev.	0.68	0.17	0.82	0.37	0.62

Table 4. Depths of the Cr-depleted and Mn-depleted zones.

Temperature of Isothermal Oxidation (°C)	Depleted Depths (µm)	
	Cr	Mn
1150	160	500
1100	85	225
1050	70	145
1000	40	85

Table 5. Mn and Cr mass lost by the alloy during oxidation.

Temperature of Isothermal Oxidation (°C)	Cr and Mn Lost by the Alloy Subsurface (mg/cm²)	
	Cr	Mn
1150	No exploitable zones	
1100	1.85 ± 0.83	10.20 ± 1.88
1050	1.17 ± 0.12	5.52 ± 1.17
1000	1.29 ± 0.22	3.92 ± 0.62

5. Discussion

Using a thermo-balance to record the mass gain every 40 s allowed observing almost continuously the progress of isothermal oxidation. The curves obtained by plotting mass gain versus time were affected by perturbations but they are all globally parabolic. The absence of significant initial linear part suggests that the isothermal transient oxidation was very short and that the specimens were very early covered all around by a continuous oxide scale which isolated them from the oxidizing atmosphere, this leading to a parabolic kinetic (Wagner's law). It was thus allowable to consider parabolic constants for all the four temperatures and to determine them. The obtained K_P values, ranging from 55 (1000 °C) to 700 (1150 °C) × 10^{-12}·g^2·cm^{-4}·s^{-1}, are considerably higher than the ones of a chromia-forming Ni–30Cr alloy, that is: from 3 (1000 °C) to 67 (1200 °C) × 10^{-12} g^2·cm^{-4}·s^{-1}·[18]. In contrast they are more or less consistent with the ones proposed by Jiang et al. [17] who found a rather high value of 465 × 10^{-12} g^2·cm^{-4}·s^{-1} at 1050 °C (this work: 85 × 10^{-12} g^2·cm^{-4}·s^{-1}) and a value of 789 × 10^{-12} g^2·cm^{-4}·s^{-1} at 1150 °C which is of the same order as the 700 × 10^{-12} g^2·cm^{-4}·s^{-1} value determined in the present work. The activation energy obtained here—270 kJ/mol—is significantly higher than the 140 kJ/mol found by Jiang et al. [17]. Surprisingly the activation energy determined here is rather close to the one for the chromia-forming Ni–30Cr alloy [18] (242 kJ/mol [18]) despite the difference of nature of the formed external oxide scales (mainly oxides of Mn, and of Mn and Cr together, and not chromia as for the Ni–30Cr alloy).

The oxides formed are numerous: oxides of Mn (seemingly MnO_2, Mn_3O_4) and of both Mn and Cr (spinel $MnCr_2O_4$ and more generally $(Mn,Cr)_xO_y$). In addition to these oxides, Jiang et al. [17] reported, after 100 h at 1050 and 1150 °C, the presence of iron oxides (Fe_3O_4 and spinel $MnFe_2O_4$). These oxides were not observed here.

Manganese was more involved in the oxide formation than chromium, as revealed elsewhere by the more severe impoverishment of the subsurface in Mn than in Cr, for all test temperatures. Obviously, Mn and Cr diffused from depths increasing with temperature, towards the surface of alloy/interface with the oxide scale. The oxide scale was, in all cases, richer in Mn than in Cr over the three outermost quarters of the oxide scale. Chromium was more present than manganese only in the last quarter of the scale, close to the alloy. A thin part of this innermost quarter of scale was seemingly chromia. Such repartition was previously noticed by Jiang et al. [17].

No oxide scale spallation seems to have taken place during the post-(1000 °C isothermal stage) cooling, according to thermogravimetry results (Figure 3). One may consider therefore that the whole oxide scale was observed during the post-mortem metallographic characterization. In contrast, near the end of cooling from 1050, 1100 or 1150 °C, spallation occurred and the outermost part of the scale was not longer available for post-mortem characterization. This explains why the thickness of the scale formed at 1100 °C (Figure 5) is equivalent to (and even a little lower than) the one after oxidation at 1000 °C for the same duration, despite a final mass gain clearly higher (Figure 1). The cross-sectional SEM observations carried out on the oxide scales formed over the surfaces of the samples oxidized at 1050, 1100 and 1150 °C are thus necessarily incomplete. For instance, the SEM/BSE images, elemental maps and concentration profiles (Figures 5, 7 and 8) corresponding to the 1100 °C-oxidized state are to be compared more to the internal part of the oxide scale developed at 1000 °C. So, it seems that the scales remaining on the surfaces of the samples oxidized at more than 1000 °C are similar to the internal part of scale wholly conserved on the surface of the samples oxidized at 1000 °C. In other words, the (0 to 50 µm) oxide zone of the profiles presented on the right of Figure 8 (1100 °C) corresponds to the (20 to 60 µm) oxide zone of the profiles given in the left side (1000 °C) of the same figure.

Manganese is the element which took part the most in the oxidation of the alloy, as shown by its predominant presence in the oxide scales and by the particularly severe Mn-impoverishment of the subsurface. Looking to the Ellingham diagram of oxides, the free energy of MnO formation in the (1000–1200 °C) temperature range is lower than the ones of formation of Cr_2O_3, of FeO, CoO, NiO and Fe_2O_3. Manganese oxides are thus expected to form early, at the expense of the oxides of the other elements of the alloy. After a MnO growth in quantity high enough, the resulting Mn-impoverishment of the alloy subsurface favors the formation of Cr_2O_3 at the scale/alloy interface, which induces itself an impoverishment in Cr in the subsurface. Oxidation at the scale/interface may become possible again, with as result the MnO formation between chromia and alloy, followed by the reaction between the two oxides according to $Cr_2O_3 + MnO \rightarrow MnCr_2O_4$. Concerning the outermost MnO part of the scale, with the decrease in Mn feeding due to the now thick oxide scale, oxygen may re-oxidize MnO into Mn_3O_4/Mn_2O_3 then MnO_2.

Beside the surface reactions, two other curious phenomena also occurred during the 50 h of the oxidation tests in the (1050, 1150 °C) range of isothermal temperatures: the precipitation of acicular particles rich in chromium and the local internal progress of oxidation. These two phenomena, also reported by Jiang et al. [17], are more or less extended depending on temperature. The precipitation of Cr-rich needles was limited to rare areas in the bulk of the specimen oxidized at 1050 °C while it was much denser and homogeneously distributed in the bulk after oxidation at 1100 °C. The progress of internal oxidation, identified by Jiang et al. [17] as being intergranular, was not observed here after 50 h at 1000 °C. In contrast, it is much more visible for 1050 and 1100 °C, and generalized to the whole specimen thickness for 1150 °C. The specimen oxidized at 1150 °C is crossed by a real network of thick oxidized interfaces. This one appears as similar to the network of oxidized cracks due the mechanical deformation at elevated temperatures during flexural creep tests (oxidized cracks during the tertiary phase of creep), whereas the specimen was here absolutely not subjected to stresses. Clearly, such oxidation behavior is catastrophic for mechanical resistance in case of applied stresses at the same time.

To finish, some comments can be done concerning the behavior in oxide scale spallation during cooling. Despite the low quality of the external oxides scales (porosities, small cracks) the specimen oxidized at 1000 °C did not suffer oxide detachment during cooling. This was not the case of the ones oxidized at 1050 and 1100 °C which started to be affected by scale spallation when temperature became lower than 400 °C. This is certainly due to the thicker oxide scales which isothermally formed at these higher temperature (according to the isothermal mass gains). Spallation was the main reason of the apparently thinner scales observed for these two specimens. The specimen oxidized at 1150 °C was logically more oxidized than the three former ones (confirmed by the corresponding isothermal mass gain) but it was not affected by scale spallation during cooling. Two explanations can be proposed: first a significant part of oxidation was internal, and second these internal oxides may improve the adherence of the external oxide scale by a pinning effect.

6. Conclusion

Testing the Cantor's alloy in high temperature oxidation using a thermo-balance allowed confirming the parabolic character of the oxidation kinetic, but it also revealed some irregularities in the isothermal mass evolution. Post-mortem characterization led results which are consistent with the phenomena previously seen by other researchers (multi-layers constitution of the external scales, precipitation of second phase in the bulk, severe internal oxidation along grain boundaries). These post-mortem results help to interpret the mass variations observed during the isothermal oxidation as well as during the following cooling. Anyhow, it is evident that the Cantor's alloy behaves too badly in oxidation to serve as a base for new metallic materials claiming to represent alternative solutions to superalloys allowing a lower dependence on critical elements. Decreasing the Mn content, an element which plays a more important (and detrimental) role in oxidation than chromium, is expected to improve the behavior. This can be done, for instance, by increasing the iron and chromium contents instead. These are ways to be explored prior to further developments for mechanical properties enhancement.

Author Contributions

Conceptualization, P.B.; Methodology, P.B. and L.A.; Software, L.A.; Validation, P.B.; Formal Analysis, P.B.; Investigation, P.B.; Resources, L.A.; Data Curation, P.B.; Writing – Original Draft Preparation, P.B.; Writing – Review & Editing, P.B.; Visualization, P.B.; Supervision, P.B.; Project Administration, P.B.; Funding Acquisition, Not applicable.

Ethics Statement

Not applicable.

Informed Consent Statement

Not applicable.

Funding

This research received no external funding.

Declaration of Competing Interest

The authors declare that they have no known competing financial interests or personal relationships that could have appeared to influence the work reported in this paper.

References

1. Cantor B, Kim KB, Warren PJ. Novel Multicomponent Amorphous Alloys. *Mater. Sci. Forum* **2002**, *386–388*, 27–32.
2. Cantor B, Chang ITH, Knight P, Vincent AJB. Microstructural Development in Equiatomic Munlticomponent Alloys. *J. Mater. Sci. Eng. A* **2004**, *375–377*, 213–218.
3. Yeh JW, Chen SK, Lin SJ, Gan JY, Chin TS, Shun TT, et al. Nanostructured High-Entropy Alloys with Multiple Principal Elements: Novel Alloy Design Concepts and Outcomes. *Adv. Eng. Mater. A* **2004**, *6*, 299–303.
4. Yeh JW, Lin SJ, Chin TS, Gan JY, Chen SK, Shun TT, et al. Formation of Simple Crystal Structures in Cu-Co-Ni-Cr-Al-Fe-Ti-V Alloys with Multiprincipal Metallic Elements. *Metall. Mater. Trans. A* **2004**, *35*, 2533–2536.
5. Hsu CY, Yeh JW, Chen SK, Shun TT. Wear Resistance and High-Temperature Compression Strength of Fcc CuCoNiCrAl0.5Fe Alloy with Boron Addition. *Metall. Mater. Trans. A* **2004**, *35*, 1465–1469.
6. Huang PK, Yeh JW, Shun TT, Chen SK. Multi-Principal-Element Alloys with Improved Oxidation and Wear Resistance for Thermal Spray Coating. *Adv. Eng. Mater.* **2004**, *6*, 74–78.
7. Kofstad P. *High Temperature Corrosion*; Elsevier Applied Science: London, UK; 1988.
8. Young DJ. *High Temperature Oxidation and Corrosion of Metals*; Elsevier Corrosion Series: Amsterdam, The Netherlands; 2008.
9. Sims CT, Hagel WC. *The Superalloys*; Wiley: New York, NY, USA; 1972.
10. Donachie MS, Donachie SJ. *Superalloys: A Technical Guide*, 2nd ed; ASM International: Materials Park, OH, USA; 2002.

11. Berthod P. As-Cast Microstructures of High Entropy Alloys Designed to Be TaC-Strengthened. *J. Met. Mater. Res.* **2022**, *5*, 1–10.
12. Berthod P. As–cast Microstructures of HEA Designed to be Strengthened by HfC. *J. Eng. Sci. Innov.* **2022**, *7*, 305–314.
13. Berthod P. Strengthening Against Creep at Elevated Temperature of HEA Alloys of the CoNiFeMnCr Type Using MC Carbides. In Supplemental Proceedings of the 152nd TMS Annual Meeting and Exhibition TMS 2023, San Diego, CA, USA, (19–23 March 2023).
14. Laplanche G, Volkert UF, Eggeler G, George EP. Oxidation Behavior of the CrMnFeCoNi High Entropy Alloy. *Oxid. Met.* **2016**, *85*, 629–645.
15. Stephan-Scherb C, Schulz W, Schneider M, Karafiludis S, Laplanche G. High-Temperature Oxidation in Dry and Humid Atmospheres of the Equiatomic CrMnFeCoNi and CrCoNi High- and Medium-Entropy *Alloys. Oxid. Met.* **2021**, *95*, 105–133.
16. Buerckner ML, Mengis L, White EMH, Galetz MC. Influence of Copper and Aluminum Substitution on High-Temperature Oxidation of the FeCoCrNiMn "Cantor" Alloy. *Mater. Corros.* **2023**, *74*, 79–90.
17. Jiang D, Li Z, Xu J, Ren Q, Agbedor SO, Lei Q. High-Temperature Oxidation Behaviors of an Equiatomic CrMnFeCoNi High Entropy Alloy. Mater. *Today Commun.* **2022**, *32*, 104185.
18. Berthod P. Kinetics of High Temperature Oxidation and Chromia Volatilization for a Binary Ni-Cr Alloy. *Oxid. Met.* **2005**, *64*, 235–252.